

LOW THERMAL CONDUCTIVITY VAPOR DEPOSITED ZIRCONIA MICROSTRUCTURES

D.D. Hass, A.J. Slifka* and H.N.G. Wadley

Department of Materials Science
School of Engineering and Applied Science
University of Virginia, Charlottesville, VA 22903 U.S.A.

*National Institute for Standards and Testing
Materials Reliability Division
Boulder, CO 80303-3337

ABSTRACT

Low thermal conductivity 7wt.% yttria stabilized zirconia (7YSZ) coatings have been grown using a low vacuum (0.20 Torr) electron beam evaporation process. In this approach, a transsonic helium jet was used to entrain and transport an evaporated 7YSZ flux to a substrate. The interaction of the helium jet with the coating surface resulted in many of the evaporated species making oblique angles of contact with the substrate. This resulted in the formation of a highly porous, columnar microstructure without substrate rotation. When the substrate was positioned perpendicular to the axis of the jet, coatings with intercolumnar pores normal to the substrate surface were formed. The ambient temperature thermal conductivity of a coating grown in this arrangement was 1.9 Wm/K, comparable to that of conventional, high vacuum electron beam coatings. When the column and pore orientation was inclined (by tilting the substrate) the thermal conductivity was observed to fall. By alternating the inclination angle as growth progressed, coatings containing zig-zag columns and pores could be synthesized. Using this technique, 7YSZ coatings with thermal conductivities as low as 0.8 W/mK were obtained. The observed thermal conductivity reduction arises from the longer thermal diffusion path of the zig-zag pore microstructures.

1. INTRODUCTION

Yttria stabilized zirconia coating systems are widely used for the thermal, oxidation and hot corrosion protection of high temperature components used in gas turbine and diesel engines[1]. These coatings are used to reduce the operating temperature and oxidation rate of metal components, and so delay the onset of the thermally induced failure mechanisms (i.e creep rupture, thermal fatigue and oxidation) that effectively govern component durability and life. For reliable thermal and oxidation protection excessive thermomechanical loading of the coating system and the metal component to which it is applied must be limited.

The multifunctional requirements of this coating application dictate the use of a coating system consisting of three separate layers[2]. A porous, 7wt% yttria stabilized zirconia (7YSZ) thermal barrier coating (TBC) which provides thermal insulation. A thermally grown (α -alumina) oxide (“TGO”) layer which inhibits oxygen transport to the component and an underlying platinum aluminate or MCrAlY (where M is Ni or Co) bond coat which is used to form the TGO layer[3,4]. The TBC layer is deposited either by air plasma spray (APS)[5] or electron beam physical vapor deposition (EB-PVD)[6]. Low pressure plasma spray (LPPS)[4] or pack cementation[7] is used to apply the bond coat. Oxidation of the bond coat prior to or during deposition of the TBC layer (and latter during service) forms the thin ($\sim 1\mu\text{m}$) TGO layer.

Yttria stabilized zirconia is the currently preferred TBC layer material for gas turbine engine applications because of its low thermal conductivity, κ , its relatively high (compared to other ceramics) thermal expansion coefficient and its good erosion resistance[8]. The low thermal conductivity of bulk YSZ is a result of the low intrinsic thermal conductivity of zirconia and the addition of yttria. Yttria additions require the creation of O^{2-} vacancies to maintain the electrical neutrality of the ionic lattice. Both the yttrium solutes and the O^{2-} vacancies are effective at reducing thermal transport and thus the thermal conductivity of YSZ decreases with increased yttria content[9,10]. A yttria concentration in the range of 6 to 8 wt.% is generally used. At this composition the spallation life of the TBC is maximized due to the formation of the metastable t' phase.

This phase yields a complex microstructure (containing twins and antiphase boundaries) which resist crack propagation and transformation into the monoclinic phase (4% volume change) upon cooling[8]. The result is a thermomechanically tough TBC layer with a room temperature, grain size dependent, thermal conductivity of 2.2-2.6 W/mK in the densest form[11].

The thermal protection and spallation lifetimes (defined by the number of thermal cycles to failure) of TBC layers produced via EB-PVD and APS are significantly different. TBC coatings produced by APS have a thermal conductivity in the range of 0.8-1.0W/mK at 25°C[1,9,12-14]. This is significantly lower than the 1.5-1.9 W/mK reported for EB-PVD coatings at 25°C[1,15]. The APS coatings therefore provide superior thermal protection. Their use is, however, limited by their poorer spallation resistance[16]. EB-PVD TBC layers have much longer (8 to 10 times) spallation lifetimes than their APS counterparts and as a result EB-PVD TBCs are preferred for aero gas turbine applications where extreme thermal cycling occurs[1].

The thermal and mechanical property differences of YSZ coatings synthesized by these two processing routes predominantly results from differences in the morphology of the porosity present within the TBC layer, Fig. 1. In APS layers, inter-splat pores result from the impingement of molten droplets onto a substrate. These pores are generally aligned parallel to the substrate surface and are accompanied by micro-cracks and fine grain boundaries, Fig. 1a. In this case, the pores provide a high impedance to heat flow through the thickness of the coating resulting in a TBC with low thermal conductivity. The spallation life of these coatings is believed to be determined by from a combination of the disc-like coating “defects” and the significant coefficient of thermal expansion (CTE) mismatch between the TBC layer and the underlying substrate. The CTE of YSZ is approximately $5 \times 10^{-6} \text{ }^\circ\text{C}^{-1}$ smaller than that of the nickel superalloys to which it is applied. During thermal cycling, stresses are formed which lead to the initiation of cracks in the TBC layer. These cracks eventually result in the premature spallation of the coating[17]. Such failures limit the use of these coatings to applications where only moderate thermal cycling is experienced (eg. land base power generation turbines)[18].

The TBC layers produced by EB-PVD have a columnar microstructure with elongated intercolumnar pores that become predominantly aligned perpendicular to the plane of the coating as its thickness increases[19]. A finer distribution of intracolumn pores also exist. The elongated intercolumnar pores increase the compliance of the coating in the direction parallel to the substrate which lowers thermal mismatch stresses and leads to improved spallation lifetimes in the TBC. For the deposition temperatures typically employed to obtain proper coating adhesion (i.e. $T/T_m \sim 0.5$ where T is the substrate temperature and T_m is the melting point of the deposited material), substrate rotation is required to obtain significant inter and intracolumnar porosity. This rotation leads to flux shadowing and a varying deposition rate. The result is the competitive growth of tapered, poorly bonded columns aligned perpendicular to the substrate surface and the finer intracolumnar pores, Fig. 1b. The perpendicular intercolumnar pores are not effective at reducing heat transfer through the thickness of the coating. However, the intracolumnar pores contribute a moderate reductions to the thermal conductivity as they are generally aligned away from the substrate normal. Even so, EB-PVD coatings have a considerably higher thermal conductivity than their APS counterparts.

Failure in these coatings no longer occurs within the TBC layer but at the TGO/bond coat interface[20]. Clarke and Christensen[21,22] have measured large residual compressive stresses (3 to 4 GPa) in the TGO layer which result from the CTE mismatch between the TGO and the substrate/bond coat ($\Delta CTE \sim 9-10 \times 10^{-6} \text{ } ^\circ\text{C}^{-1}$) and growth stresses in the TGO. Evans et.al.[23,24] have analyzed the thermomechanical stresses and show that they lead to the initiation of cracks along the TGO/bond coat interface. Out-of-plane tensile stresses resulting from undulations or morphological defects that form on an otherwise smooth surface[23], ratcheting effects caused by cyclic plasticity in the substrate[24] and TGO/bond coat interface embrittlement (due to sulfur impurities)[24,25] have all been conjectured to play a role in the failure of EB-PVD TBC's[26,27]. Control of TGO failure mechanisms is clearly a critical issue for the development of more durable TBC systems.

One approach to improve TBC system performance is to optimize the pore morphologies in order to reduce the TBC thermal conductivity while still retaining a high in-plane compliance. Lower thermal conductivities lead to temperature reductions at the TGO bond coat interface which slows the rates of the thermally induced failure mechanisms. For example, lower temperatures in the bond coat/TGO would reduce the CTE mismatch strain in the TGO layer, slow the growth rate of the TGO layer and retard impurity diffusion within the bond coat. Alternatively, lower thermal conductivity layers might allow designers to reduce the TBC thickness and in doing so decrease the significant centrifugal load that the mass of the TBCs imposes on the rotating turbine engine blades components[28].

Robbie et.al.[29] recently used an electron beam evaporation process and a highly inclined substrate to condense vapor flux and grow thin (1-5 μm thickness) films of copper, chromium and magnesium fluoride with inclined intercolumnar pores. Zig-zag shaped pores were also demonstrated. In this case the adatom angle of incidence is altered by inclining the substrate between two fixed angles, so that the inclination angle of the substrate with respect the source was greater than $\sim \pm 70^\circ$. By altering the inclination angle and the dwell time at each position, films with a low relative density (porosity up to 85%) and zig-zag pore morphologies were produced[30]. Since the thermal conductivity of thin films is well known to be strongly effected by the relative volume fraction and morphology of the porosity present[31,32], such approaches are of interest in thermal protection applications where films containing pores optimized to reduce heat transfer are desired. However, the conventional EB-PVD process used in this approach has a low intrinsic materials utilization efficiency (MUE, defined as the percentage of the evaporated flux which is deposited onto the substrate) which results from the vapor expanding from the source with an angular flux distribution that is described by a $\cos^n(\theta)$ function (where $n=2,3,4$ or more)[33]. By using a highly inclined substrate (70° or greater) to obtain an oblique vapor incidence, a further reduction in the MUE occurs resulting in a very low deposition rate (0.2-0.4 $\mu\text{m min.}^{-1}$)[30]. This is more than an order of magnitude less than that used in conventional EB-PVD processing[19], and would result in a very uneconomical process.

One approach for improving the deposition efficiency of electron beam evaporation is the use of an electron beam directed vapor deposition (EB-DVD) process[34]. This approach employs electron beam evaporation and a transsonic helium gas jet into which the vapor is entrained and deposited onto a substrate. This process can be designed to have a very large (60 to 80%) MUE leading to high ($>20\mu\text{m min}^{-1}$) deposition rates, even with low power evaporation sources. Recent atomic transport modeling[35] indicates that the interaction of the helium jet with the substrate results in many oblique angle impacts and the growth of highly porous, columnar coatings without the need for substrate rotation[36]. Here, we couple this approach with substrate manipulation to create coatings with zig-zag column morphologies, like those in Fig. 2, using high deposition rates ($3.0\text{-}5.0\ \mu\text{m min}^{-1}$). It will be shown that this results in TBC layers with a greatly reduced thermal conductivity.

2. Experimental

2.1 *Electron Beam Directed Vapor Deposition*

Electron beam directed vapor deposition (EB-DVD) combines high rate, low vacuum electron beam evaporation with a rarefied gas jet to entrain vapor and transport it to a substrate[34]. The current approach uses the combination of a continuously operating 60 kV/10 kW axial e-beam gun (modified to function in a low vacuum (0.1-5.0 Torr) environment) and a He-O₂ carrier gas jet of controlled composition. A detailed description of the EB-DVD system can be found elsewhere[34,37].

During operation, a source material is vaporized and the carrier gas jet collides (at high velocity) with the resulting vapor directing it towards the substrate. Collisions in the flow cause the vapor to be scattered toward the substrate where it condenses. When all the vapor is entrained in a small ($\sim 3\text{cm}$) diameter jet, a high fraction of the evaporated flux can be deposited and high local deposition rates are achievable[34]. By altering the nozzle geometry, the upstream and chamber pressures and the evaporated flux the average incidence angle of the vapor atom/molecule flux can be

controlled. By using processing conditions in which the velocity of the carrier gas stream has a substantial component in the direction parallel to the surface of the substrate (i.e. a wall jet) off-normal incidences are promoted. Under such conditions, significant flux shadowing occurs without rotation leading to columnar morphologies having significant intercolumnar pores with widths up to $1\mu\text{m}$ [35].

Inclined column morphologies were produced here by inclining the substrate away from the jet axis by an angle θ , Fig. 3. This resulted in the growth of columns inclined to the substrate normal by an inclination angle, ω , where $\omega < \theta$. Zig-zag column morphologies were produced by depositing vapor at a high θ value (typically 45°) for a prescribed dwell time, then rotating to $-\theta$, and depositing for the same dwell time. The “zig-zag” wavelength, λ , (defined as the coating thickness produced in one $\pm \theta$ cycle) was controlled by the dwell time and the YSZ evaporation (and thus deposition) rate.

2.2 Thermal Barrier Coating Deposition

The EB-DVD approach was used to deposit 7YSZ layers on (i) a stationary substrate aligned perpendicular to the direction of the vapor flux, (ii) a stationary substrate inclined 45° away from the direction of the vapor flux, and (iii) on substrates that were oscillated using the dwell cycles described above. The evaporation source was a $\sim 70\%$ dense, $\text{ZrO}_2\text{-}7.13\text{ wt.\%Y}_2\text{O}_3$ cylindrical ingot prepared by Trans-Tech, Inc.(Adamstown, MD). A 1.2 kW electron beam with a $\sim 3\text{mm}$ spot size and a 10Hz scan rate was used for evaporation. The evaporated flux was entrained in a 8.0 standard liter per minute (slm) helium-3.0vol.% oxygen gas flow and deposited on 2.54 cm diameter discs of IN100 coated with a nickel aluminide bond coat supplied by GE Aircraft Engines. The oxygen in the gas flow compensated for oxygen depletion in the ceramic source during evaporation[6]. For all experiments, the substrate was positioned 10.0 cm from the nozzle and 7.6 cm from the source. A resistive heating source was used to raise the substrate to a temperature of $\sim 1030^\circ\text{C}$ ($\pm 25^\circ\text{C}$). This was monitored using a thermocouple inserted in a hole drilled in the

side of the substrate and centered with respect to the substrate thickness. The coating thickness, deposition rate and substrate manipulation strategies employed are summarized in Table I.

3. Coating Morphology

All layers deposited using EB-DVD exhibited a columnar structure with some porosity in the form of elongated pores that extended from the substrate to the top of the coating. The porosity was “heirarchical” in nature, Fig. 4. Three distinct pore scales were found and are schematically illustrated in Fig. 2. The largest (Type I) existed between the primary growth columns that were 9.8 - 58.8 μm in width. The resulting intercolumnar pores had a typical width in excess of 0.3 μm . Narrower, often discontinuous, but still elongated Type II pores existed between intermediate columns that were 0.6 - 2.5 μm in width. The thinner Type II pores had a width of ~0.1 μm . The finest observable growth columns (20 - 80nm in width) had elongated, Type III pores ~ 20nm wide. The pore spacing, ϵ , the pore width, ρ , the pore inclination angle, ω , the zig-zag wavelength, λ , and the zig-zag amplitude, a , (as defined in Fig. 2) were measured. The average values are summarized for the Type I, II, and III pores in Tables 2, 3 and 4. The coating morphology for the six coatings is shown in cross section in Fig. 5. The surfaces of each coating are shown in Fig. 6.

3.1 Substrate perpendicular to the jet axis (Sample A)

Figs. 5a and 6a show the structure of an EB-DVD coating deposited onto a substrate that was aligned perpendicular to the jet axis. A coating with a columnar morphology resulted. The largest observed columns were defined by Type-I pores spaced an average of 14.9 μm apart. The columns had symmetrical shaped domed tops and the column growth direction was parallel to the substrate normal. The average Type-I pore width, ρ , was 0.4 μm . Type-II pores were not observed, however, fine columns defined by Type-III pores were present. They were closely spaced an average of 60nm apart and were also orientated parallel to the substrate normal. Note that the width of the primary growth columns did not vary through the coating thickness. This is consistant with previ-

ous observations of EB-DVD coatings and is distinctly different to the morphology of EB-PVD coatings where competitive column growth occurs and results in tapered columns[38].

3.2 Substrate inclined 45° to the jet axis (Sample B)

In Figs. 5b and 6b the morphology of a coating deposited on a substrate inclined at 45° to the jet axis is shown. Type-I pores were irregularly dispersed throughout the sample. The Type-II pores were present and were on average spaced 1.5μm apart. The columns defined by the Type-II pores had domed tops and again exhibited (noncompetitive) parallel growth. Type-III pores were also present. These pore were spaced approximately 70nm apart. All the pores were, on average, inclined 44° away from the substrate normal.

3.3 Oscillatory substrate inclination (Samples C,D,E,F)

Figs. 5(c-f) and 6(c-f) show the morphologies of coatings grown by oscillating the substrate between +/- 45°. The dwell times at each inclination were: 300 sec. (sample C), 150 sec. (sample D), 75 sec. (sample E) and 38 sec.(sample F). This substrate manipulation approach resulted in the growth of coatings which exhibited zig-zag column and intercolumnar pore geometries. The columns were found to have ellipsoidal sections with domed tops. The elongated axis was aligned parallel to the direction of the vapor flux [Fig. 5(c-f)]. In all samples the primary growth columns remained uniform in width (noncompetitive growth) with the exception of sample F which occasionally exhibited slightly tapered columns. Altering the substrate dwell time effected both the zig-zag wavelength and amplitude. The zig-zag wavelength decreased from 31 to 3μm as the deposition dwell time decreased. The Type I pore spacings and widths were not, however, observed to vary significantly, see Table 2. Note that the zig-zag samples had pore spacings and widths nearly twice those of the stationary sample A. The inclination angle, ω , of the columns and intercolumnar porosity were found to vary with sample and pore type, Table 2. The Type I pores had the largest ω variation. Samples C and D had Type-I pores with inclination angles approximately twice those found in samples E and F. The smaller growth angle of the Type I pores in samples E and F along with their wide intercolumnar spacing (0.6μm) and shorter zig-zag wavelength (3 to 6μm)

resulted in the amplitude of the zig-zag pores approaching the width of the pores, Fig. 7. As a result, the Type-I pores were effectively parallel to the substrate normal for these samples. In contrast, the Type-II & III pores showed only moderate variations in ω (29° to 34°) and remained inclined to heat flow through the coating thickness.

4. Thermal Conductivity Measurement

4.1 Measurement methodology

The thermal conductivity, κ , of ceramic coatings can be measured using either a direct (steady state)[39,40,41] or an transient approach[42,43]. In the later the thermal diffusivity, α , of a material is measured and subsequently related to thermal conductivity using the relationship:

$$\kappa = \alpha \cdot C_p \cdot \rho \quad (1)$$

where C_p is the heat capacity and ρ is the density of the material. For the coatings studied here, the density and heat capacity are not well characterized. As a result, a steady-state technique was used for the thermal conductivity measurements. The technique employed an infra-red thermal microscope in conjunction with infra-red laser heating, Fig. 8, to determine the thermal conductivity of a sample using a variation of ASTM 1225-87 (commonly known as the cut-bar approach)[44]. In the cut-bar approach, a specimen of unknown thermal conductivity is sandwiched between two materials with known thermal conductivities. By applying heat in the direction parallel to the material interfaces and measuring the temperature along the length of the three materials, the heat flow, Q , may be inferred and used to determine the thermal conductivity of an unknown specimen since:

$$Q = -\kappa A \frac{\Delta T}{\Delta x} \quad (2)$$

where Q is the conducted thermal power (W), κ is the thermal conductivity (W/mK), A is the cross-sectional area that the heat flows through (m^2), and $\Delta T/\Delta x$ is the temperature gradient (K/m)

over the distance that heat flow is measured. In the approach used for this work, the temperature difference across a fixed, known distance of the substrate was measured using an IR microscope. This, in conjunction with the known thermal conductivity of the substrate material (IN100) and equation (2) was used to calculate Q. The thermal conductivity of the coating could then be determined by measuring $\Delta T/\Delta x$ across the thickness of the coating. The validity of this testing methodology has been confirmed using a guarded hot plate approach (ASTM C177-85)[45] and was useful for the present study as it directly measured the thermal conductivity of a ceramic coating, was relatively fast (guarded hot plate approaches often required greater than 130 hours to perform[46]) and could be applied to small samples (3mm x 3mm) making a study of the effect of pore morphology on the thermal conductivity of TBC layers feasible. Details of its implementation can be found in appendix I.

4.2 Thermal conductivity results

The thermal conductivity of the six EB-DVD coatings and one EB-PVD coating deposited onto a rotated substrate (provided by GE Aircraft Engines) were measured. Fig. 8, plots the measured values of thermal conductivity against the wavelength of the zig-zag pores. Also included in Fig. 8 are the literature values for bulk YSZ and TBC layers deposited using an EB-PVD and APS. The results reveal a range of thermal conductivities with the lowest value (0.8 W/m-K) found in the EB-DVD deposited zig-zag TBC layer with a 13.1 μ m wavelength. The largest thermal conductivity of 1.9 W/m-K was found in the EB-DVD layer deposited onto a stationary substrate aligned perpendicular to the vapor flux. The EB-PVD TBC was found to have a thermal conductivity of 1.6 W/m-K which was within the range of reported literature values.

5. Discussion

5.1 Effect of processing induced porosity on thermal conductivity

In dielectric solids heat is transferred via conduction either by lattice waves (phonons) or electromagnetic radiation (photons)[47]. Phonon conduction occurs for all temperatures whereas the

radiation component only becomes significant at elevated temperature. The low temperature thermal conductivity results reported here are therefore only a measure of the ease of phonon conduction. In all cases, thermal conductivities significantly below that of bulk 7YSZ were observed. This is a result of phonon scattering by grain boundaries, interfaces and porosity[48]. The extent of the thermal conductivity reduction is strongly dependent on the morphology and volume fraction of the grain boundaries and pores present after deposition. Thermal conductivities much lower than bulk values are also observed in YSZ coatings deposited using EB-PVD and APS approaches. The magnitude of this reduction varies greatly, however, due to changes in the volume fraction and morphology of the pores present[1]. As a result, control of the pore volume fraction and morphology is critical for optimizing the thermal conductivity of these coatings.

Using the EB-DVD approach and a substrate aligned perpendicular to the vapor flux (sample A) YSZ coatings with porous, columnar microstructures were produced. The observed growth columns, however, were distinctly different from those grown using conventional EB-PVD conditions. In that case, columns grow by a competitive growth mechanism that results in tapered shaped columns. In addition, the primary growth columns in EB-PVD are separated by intercolumnar pores of moderate width (typically $< 0.1\mu\text{m}$) and subdivided by finer intracolumnar porosity which is often aligned away from the substrate normal. As a result, many of the intracolumnar pores intersect the primary heat flow path. In the EB-DVD deposited coatings, competitive growth is less evident and parallel (noncompetitive) column growth is observed. The large volume fraction of oblique vapor incidence angles present in this approach lead to the formation of wide (up to $1\mu\text{m}$) intercolumnar pores (Type I). In coatings of this type a large portion of the pores (of all types) are aligned approximately perpendicular to the substrate. As a result, the pore morphology is less effective at impeding the thermal transport. The thermal conductivity of EB-DVD layers deposited on a substrate aligned perpendicular to the jet axis (1.9W/mK) is therefore higher than that of EB-PVD coatings (1.6 W/mK). It is still below that reported for bulk 7.0-8.0wt%YSZ ($2.2\text{-}2.6\text{ W/mK}$)[9].

The use of the EB-DVD zig-zag growth approach has enabled the inclination of all pores types to be manipulated. When inclined pores are present, heat is forced to diffuse along the path defined by the pores. This distance is significantly extended by the zig-zag pore morphology at each of the three length scales. The importance of these changes to the pore morphology is demonstrated by comparing the thermal conductivity of sample A to coatings deposited using the zig-zag approach. In samples B, E and F, thermal conductivities of 1.4, 1.3 and 1.4 W/m-K respectively were observed (similar to that of EB-PVD deposited 7YSZ coatings). In these samples the fine scale pores (Type II & III) had zig-zag shaped pores with a similar spacing, width and inclination. The larger scale (Type I) porosity, however, was either observed in low volume fraction (sample B) or largely aligned parallel to the heat flow direction (sample E and F). For samples E and F, the short dwell times resulted in a short zig-zag wavelength, a small zig-zag amplitude and an inclination angle which was approximately half that of the Type II & III pores (see Table 2). Under these conditions the magnitude of the zig-zag amplitude approached that of the relatively wide (0.6 μm) Type-I pores and thus the morphology of the pores was not greatly effected by the substrate manipulation cycle. The Type I pores were therefore aligned approximately parallel to the direction of the heat flux and as a result, these pores did not effectively limit the thermal transport. Thermal transport along the zig-zag shaped Type II and III pores, however, was 20% longer than in sample A which led to a more significant impedance to heat flow. The observed 0.5-0.6 W/mK conductivity reduction of these samples compared with sample A can therefore be attributed to these changes in the Type II and III pore morphologies.

The lowest thermal conductivities (0.8 and 0.9 W/mK) were seen in samples C and D. In these coatings, the Type I pores had a longer wavelength and greater inclination angle. This resulted in a pore amplitude that was much larger than the column width and Type I pores with zig-zag morphologies. The Type II & III voids in these samples were similar in scale and orientation as those observed in samples B, E and F. All the pores therefore contributed to an increased thermal diffusion path length. As a result, these coatings were very effective at limiting thermal transport. The result was a vapor deposited coating with columnar pores having a 50% lower thermal conductiv-

ity than conventionally applied EB-PVD coatings and a similar thermal conductivity to their low durability APS counterparts.

6. Conclusions

An electron beam directed vapor deposition technique has been used to grow 7YSZ coatings with porous, columnar microstructures. The process results in samples containing a hierarchy of pore sizes. Large ($\sim 0.5\mu\text{m}$ wide) Type I pores were formed between primary growth columns. Finer ($\sim 0.1\mu\text{m}$ wide) Type II pores were formed between major grains in the columns, and very small ($\sim 20\text{nm}$ wide) Type III pores were present within the grains. By manipulating the substrate inclination during growth the orientation of the pores could be varied. When all three pore types were grown normal to the substrate (no inclination) samples with high (1.9 W/mK) thermal conductivities were formed. Growth with a substrate inclination of 45° resulted in elongated Type II and III pores that were inclined to the primary heat flow direction and the thermal conductivity was reduced to 1.4 W/mK . By rocking the substrate between inclinations of 45° and -45° , zig-zag pore morphologies were created. Using this approach, all scales (Type I, II and III) of the hierarchical pore structure could be utilized to impede heat flow through the coating thickness. In this way, coatings with thermal conductivities as low as 0.8 W/mK were produced.

Acknowledgements --- The authors are grateful to Dr. Steve Fishman of the Office of Naval Research through Contract No. N00014-97-1-0106 and to the Virginia Space Grant Consortium for support of this work. They would also like to thank Dave Wortman of G. E. Aircraft Engines for providing samples and substrate material for this research.

References

1. Meier, S. M. and Gupta, D.K., *Trans. of the ASME*, 1994 **116**, 250.
2. Strangman, T.E., *Thin Solid Films*, 1985, **127**, 93.
3. Wortman, D.J., Nagaraj, B.A. and Duderstadt, E.C., *Mat. Sci. Eng.*, 1989, **A121**, 443.
4. Gell, M. et.al., *Surf. and Coat. Tech.*, 1999, **120-121**, 53.

5. Koosloos, M.F.J., van Liempd, G.G. and Houben, J. M., *Surf. Eng.*, 1998, **14** [2], 144.
6. Unal, O., Mitchell, T.E. and Heuer, A.H., *J. Am. Ceram. Soc.*, 1994, **77** [4], 984.
7. Claves, D. and Galerie, A., *J. Physique IV*, 1993, **C9**, 531.
8. Jones, R. L., NRL/MR/6170-96-7841, 1996.
9. Morrell, P. and Taylor, R., *High Temp. High Press.*, 1985, **17**, 79.
10. Klemens, P. G., *High Temp. High Press.*, 1985, **17**, 41.
11. Kyongjun, A., Ravichandran, K.S. and Semiatin, S.L., *J. Am. Ceram. Soc.*, 1999, **82** [2], 299.
12. DeMasi, J.T., Ortiz, M. and Sheffler, K.D., NASA CR 182230, 1989.
13. Miller, R.A., Leissler, G.W. and Jobe, J.M., NASA TP 3285, 1993.
14. Filla, B. J., *Rev. Sci. Instrum.*, 1997, **68**[7], 2822.
15. Portal, R., *Rapport de stage SNECMA*, 1997.
16. DeMasi-Marcin, J.T., Sheffler, K.D. and Bose, S., *J. of Eng. Gas Turbines and Power*, 1990, **112**, 521.
17. Koolloos, M.F.J. and Houben, J.M., *Proceedings of the ASM International Materials 98* (Rosemount, IL), 1998, pp.12-15.
18. Troczynski, T., Cockcroft, S. and Wong, H., *Key Eng. Mat.*, 1996 [122-124], 451.
19. Schulz, U., Oettel, H. and Bunk, W., *Z. Metallkd.*, 1996, **87**, 6.
20. Wright, P.K., *Mat. Sci. and Eng.*, 1998, **A245** [2], 191.
21. Christensen, R.J., Lipkin, D.M., Clarke, D.R. and Murphy, K., *Appl. Phys. Lett.*, 1996 **69** [24], 3754.
22. Clarke, D.R., Christensen, R.J. and Tolpygo, V., *Surf. and Coat. Tech.*, 1997, **94-95**, 89.
23. Evans, A.G., He, M.Y. and Hutchinson, J.W., *Acta Mater.*, 1997, **45** [9], 3543.
24. Evans, A.G., Hutchinson, J.W. and Wei, Y. *Acta Mater.*, **47** [15], 4093.
25. Pint, B.A., Wright, I.G. and Alexander, K.B., *Mat. Sci. and Eng.*, 1998, **A245** [2], 201.
26. Gell, M. et. al, *Metall. Mat. Trans. A*, 1999, **30**, 427.
27. He, M.Y., Evans, A.G. and Hutchinson, J.W., *Mat. Sci. and Eng.*, 1998, **A245** [2], 168.
28. Soechting, F.O., *Proceedings of TBC'95 Workshop*, 1995, 1.
29. Robbie, K. et.al., *J. Vac. Sci. Technol. A*, 1995, **13** [3], 1032.
30. Robbie, K. and Brett, M.J., *J. Vac. Sci. Technol. A*, 1997, **15** [3], 1460.
31. Furmanski, P. and Floryan, J.M., *Trans. of the ASME*, 1994, **116**, 302.
32. Hasselman, D.P.H., *J. Comp. Mater.*, 1978, **12**, 403.
33. Schiller, S., Heisig, U. and Panzer, S., *Electron Beam Technology*, John Wiley & Sons, New York, 1982, pp.175-177.
34. Groves, J.F. and Wadley, H.N.G., *Composites B*, 1997, **28B**, 57.
35. Groves, J.F., Wadley, H.N.G., Ritenour, A.P., Hass, D.D. and Ratnaparkhi, P.L., *Proceedings of Electron Beam Melting and Refining State of the Art*, Bakish Materials Corp., Englewood, NJ, 1997, pp.46-59.
36. Hass, D.D., Parrish, P.A. and Wadley, H.N.G., *J. Vac. Sci. Technol. A*, 1998, **16** [6], 3396.
37. Groves, J.F., *Ph.D. Thesis*, University of Virginia, 1998.
38. Schulz, U., Fritscher, K. and Peters, M., *Surf. Coat. Technol.*, 1996, **82**, 259.
39. Parker, W. J. et. al., *J. Appl. Phys.*, 1961, **32**, 1679.
40. Cowan, R. D., *J. Appl. Phys.*, 1962, **34**, 926.
41. Cahill, D.G., *Rev. Sci. Instrum.*, 1990, **61**, 802.
42. Weinland, C.E., *J. Am. Ceram. Soc.*, 1934, **17**, 194.
43. Kingery, W.D., *Property Measurements at High Temperature* , Wiley, New York, 1959, p.104.

44. ASTM Standard Test Method E 1225-87, *Annual Book of ASTM Standards*, ASTM, Philadelphia, 1994, **14.02**, p.712.
45. ASTM Standard Test Method C 177-85, *Annual Book of ASTM standards*, ASTM, Philadelphia, 1992, **4.06**, p.17.
46. Slifka, A.J., Filla, B.J. and Phelps, J.M., *Proceedings of the 1997 TBC Workshop*, Cincinnati, OH, 1997, pp.33-39.
47. Kingery, W.D., Bowen, H.K. and Uhlmann, D.R, *Introduction to Ceramics*, Wiley, New York, 1976, p.583.
48. Klemens, P.G., *Mat. Sci. and Eng.*, 1998, **A245**, 143.

Appendix I.

An infra-red thermal microscope in conjunction with infra-red laser heating was used to determine the thermal conductivity of a sample using a variation of ASTM 1225-87. The infrared microscope was used to measure the temperature at various points on the coating and substrate. It had a single detector and was sensitive to a range of wavelengths (8 to 12 μm) was. An internal rotating mirror was used to scan the thermal image across the detector. One side of the coating was polished and coated with carbon to give a flat surface with uniform emissivity. Then the substrate side of the specimen was attached to a water cooled copper block using a cyanoacrylate adhesive. The specimen was heated by means of a laser which provided an efficient noncontact source of heat. The desired heating power was about 0.5 to 1 W flowing through the specimen. This was achieved using a computer controlled Invar-stabilized laser to heat the TBC coating. This provided repeatability between successive runs (this laser offered less than 2% variation over the 30 minute duration of a test) and the stability necessary for the heat-flow to achieve steady-state. The laser beam was defocussed, or expanded, and then limited by an aperture to produce a spot that covered the entire end of the specimen and thereby provided uniform heating. Heat flowing through the coating to the substrate was conducted away from the copper block by the cooling water. The infrared microscope had a very short depth of field (about 10 μm) and experiments showed that the measured temperatures was sensitive to focus as temperature differences of 25% occurred when the image was moved 30 μm out of focus. A specimen stage was therefore designed to allow for focussing within 10 μm of apparent correct focus as defined by the observer.

Experiments showed that changes of 10 μm from the apparent correct focus did not change the recorded temperature significantly. The infrared microscope, laser, and beamline optics were set up on an optical table to reduce vibration that would cause additional apparent thermal noise. The infrared scanning system allowed temperature sensors to be placed, via software, on the field of view in increments of 11 μm . These temperature spots were not physical sensors, but rather a software device that measured the temperature of a single pixel in the scanned field-of-view. The temperature spots could be placed at precise x-y coordinates allowing the software temperature sensors to be repeatably placed at fixed distances, two or more on the coating and two or more on the substrate. The consistency of the data was checked by placing more than two temperature spots on the coating and substrate. The greater the spot spacing, the greater the temperature difference between temperature spots and, hence, the greater the precision of the measurement. The temperatures of the four spots were measured at a rate of 6 to 25 times per second for 30 minutes. This stream of temperature data was used to verify steady-state temperature during the test. The data were averaged to determine precise temperatures and then used to determine κ .

7. Figure Captions

- Figure 1 Schematic illustrations of the pore morphology of (a) a plasma spray deposited YSZ showing its coarse, disc-like pore aligned parallel to the substrate surface and (b) an electron beam physical vapor deposited YSZ coating with elongated pores aligned perpendicular to the substrate surface.
- Figure 2 Schematic illustration of the pore morphology present in the zig-zag coating concept explored in this paper.
- Figure 3 Schematic illustration of the use of EB-DVD methods to deposit 7YSZ layers with a zig-zag columns and intercolumnar pores
- Figure 4 Micrographs showing the hierarchical columnar microstructures found in a EB-DVD thermal barrier coatings. This sample had a zig-zag coarse pore morphology with a 3.14 μm wavelength (sample F).
- Figure 5 Micrographs of EB-DVD coating cross sections. The columns in A) are aligned perpendicular to the substrate. In B) the columns are aligned at 45 $^{\circ}$ to the substrate normal. In C) through F) coatings with “zig-zag” column morphologies are shown with wavelengths of C) 31.7 μm , D) 13.41 μm , E) 6.57 μm and F) 3.14 μm . All coatings were deposited with an upstream pressure of 1.90 Torr, a 0.19 Torr chamber pressure and a 1030 $^{\circ}\text{C}$ substrate temperature.
- Figure 6 Micrographs of the surface of the EB-DVD thermal barrier coatings.
- Figure 7 Schematic illustrations and micrographs showing the change in the average pore wavelength, amplitude and inclination of samples C, D, E, and F
- Figure 8 Schematic illustration of the infra-red thermal conductivity approach used to measure thermal conductivity.
- Figure 9 Measured room temperature thermal conductivity of the EB-DVD thermal barrier coatings. Also shown is our measurement of an EB-PVD sample. The range of literature thermal conductivity values for plasma spray, EB-PVD and bulk 7-8YSZ are shown on the right.

Table 1: Processing Conditions Used for EB-DVD Coatings

Sample	Chamber Pressure, P_o (Torr)	Upstream Pressure, P_u (Torr)	Deposition Rate ($\mu\text{m}/\text{min.}$)	Substrate Angle(θ) (degrees)	Dwell Time (seconds)	Coating Thickness (μm)
A	0.19	1.90	10.0	0	-----	95
B	0.19	1.90	5.0	45	-----	96
C	0.19	1.90	3.2	+/- 45	300	76
D	0.19	1.90	3.0	+/- 45	150	66
E	0.19	1.90	3.0	+/- 45	75	78
F	0.19	1.90	3.0	+/- 45	37	76

Table 2: Type I pore morphology parameters for EB-DVD deposited coatings

Sample	Wavelength, λ (μm)	Amplitude, a (μm)	Pore Inclination, ω (degrees)	Pore Spacing, ϵ (μm)	Pore Width, ρ (μm)
A	∞	-----	0	14.9	0.4
B	192	92.7	44.6	discontinuous	-----
C	31.7	9.6	31.1	26.1	0.6
D	13.4	4.4	33.5	34.9	0.7
E	6.6	0.9	16.5	25.3	0.6
F	3.1	0.4	14.8	29.3	0.6

Table 3: Type II pore morphology parameters for EB-DVD deposited coatings

Sample	Wavelength, λ (μm)	Amplitude, a (μm)	Pore Inclination, ω (degrees)	Pore Spacing, ε (μm)	Pore Width, ρ (μm)
A	∞	-----	-----	-----	-----
B	192	92.7	44.6	1.5	~0.1
C	31.7	10.5	33.4	1.8	~0.1
D	13.4	4.4	33.4	1.0	~0.1
E	6.6	2.2	34.2	1.6	~0.1
F	3.1	0.9	29.8	1.4	~0.1

Table 4: Type III pore morphology parameters for EB-DVD deposited coatings

Sample	Wavelength, λ (μm)	Amplitude, a (μm)	Pore Inclination, ω (degrees)	Pore Spacing, ε (nm)	Pore Width, ρ (nm)
A	∞	-----	0	60	~20
B	192	92.7	44.6	70	~20
C	31.7	10.5	33.4	30	~20
D	13.4	4.4	33.4	40	~20
E	6.6	2.2	34.2	40	~20
F	3.1	0.9	29.8	30	~20

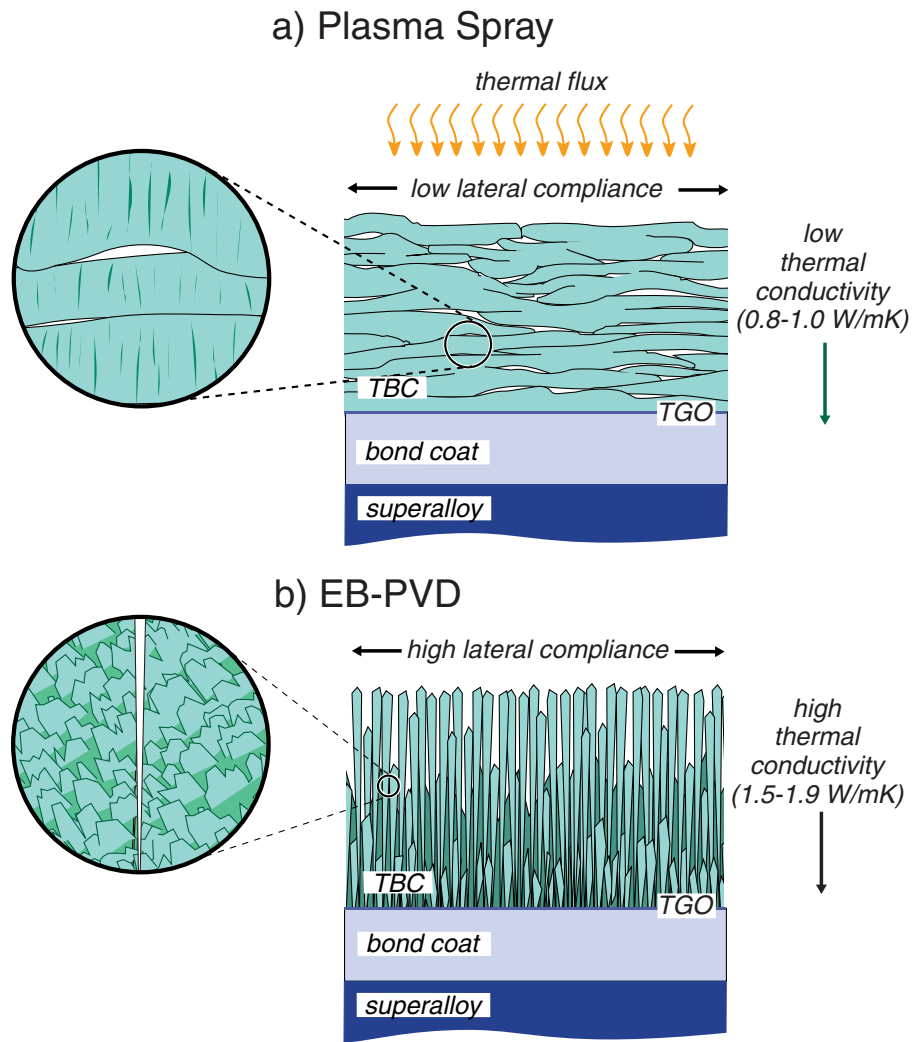


Fig. 1

EB-DVD "Zig-Zag" Coating Concept

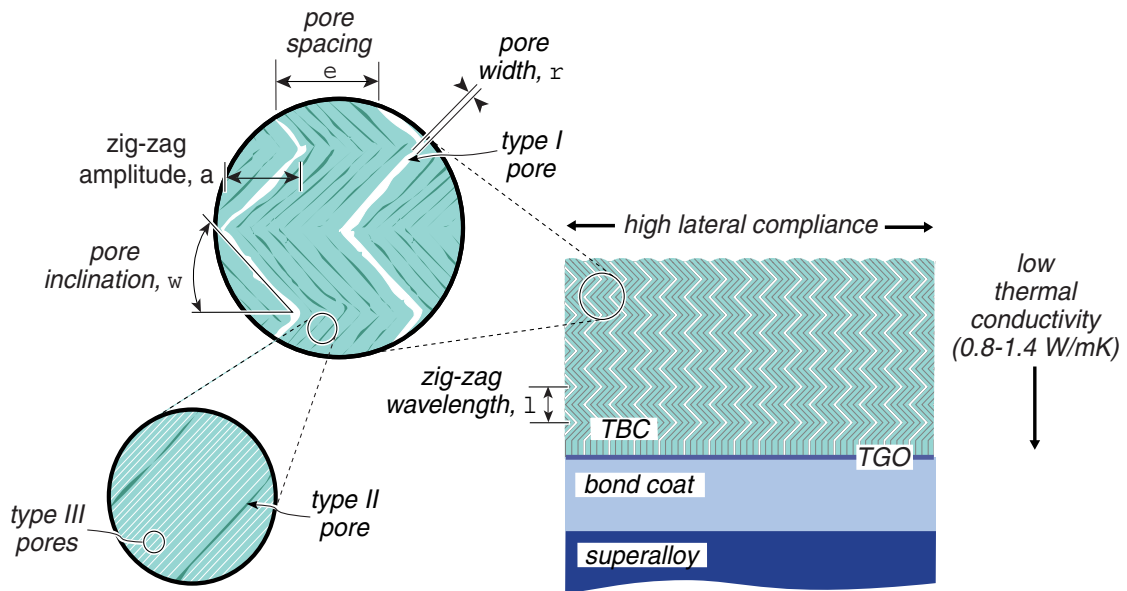


Fig. 2

EB-DVD Processing Approach

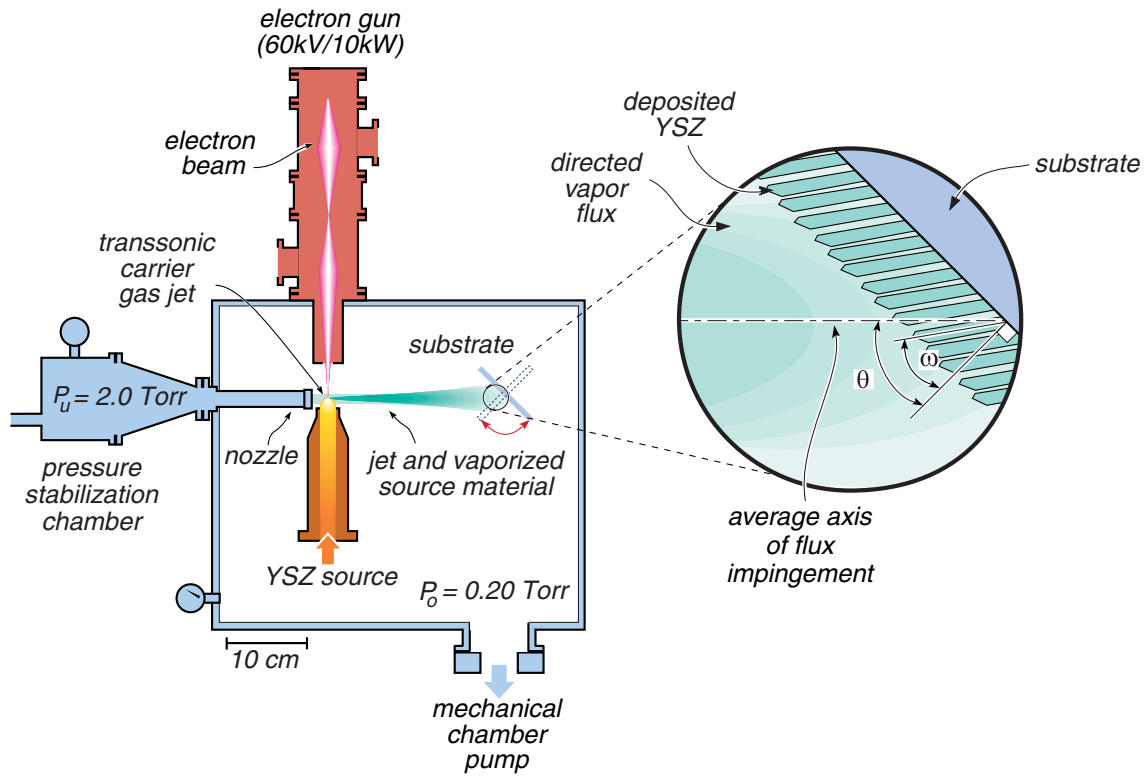


Fig. 3

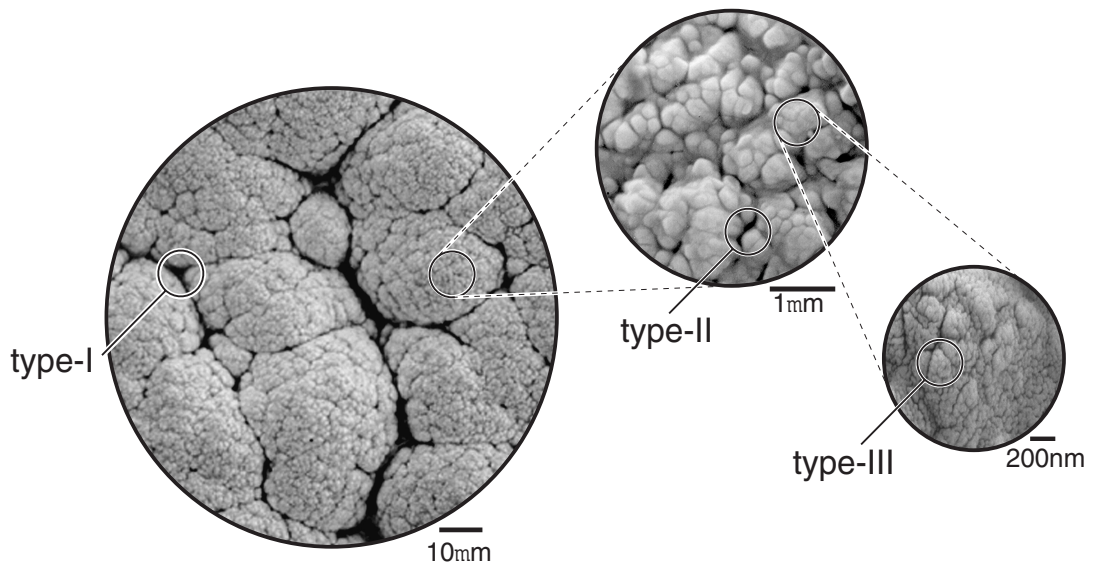


Fig. 4

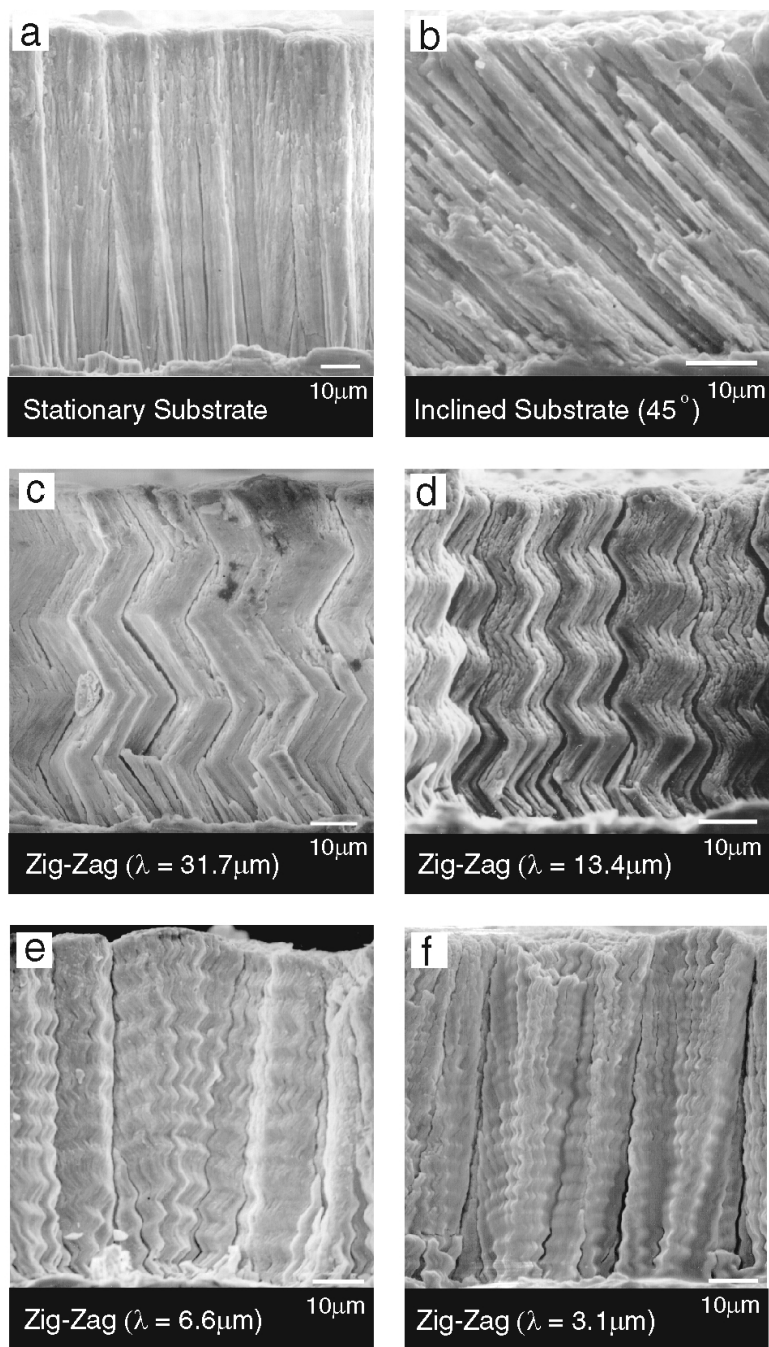


Fig. 5

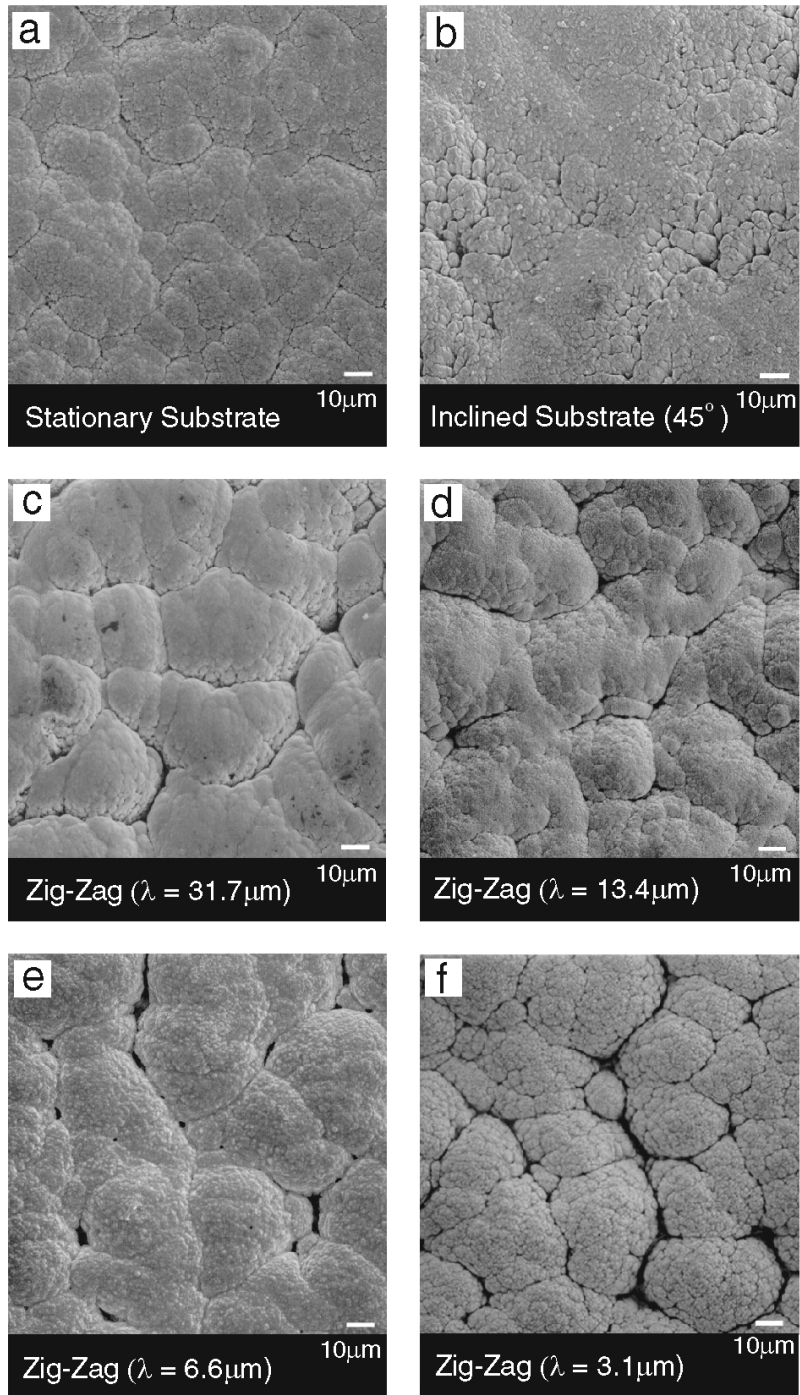


Fig. 6

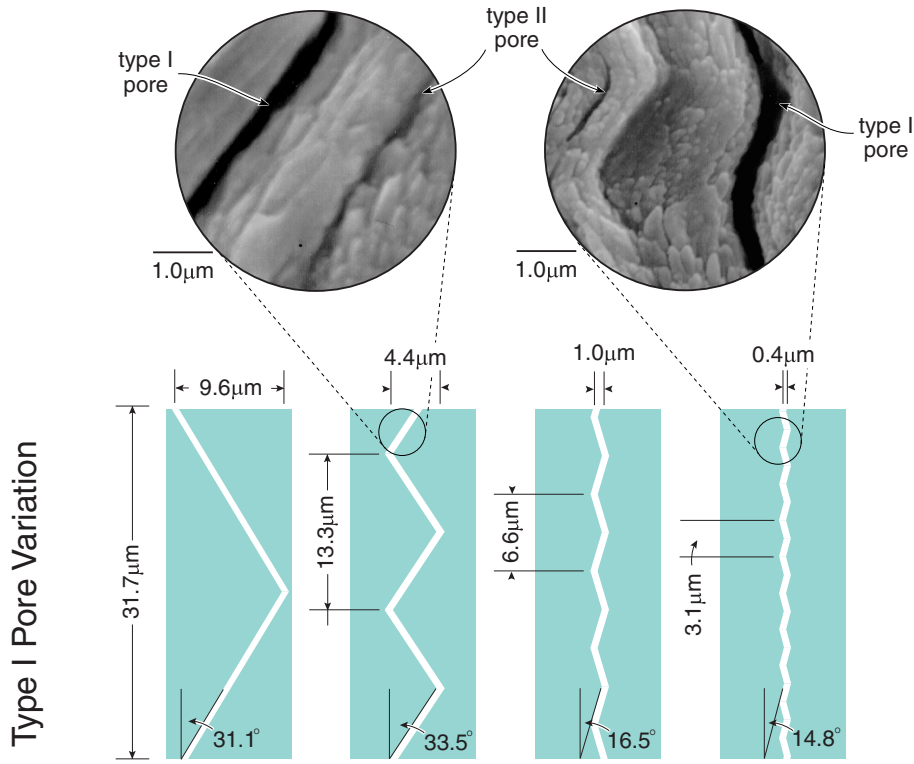


Fig. 7

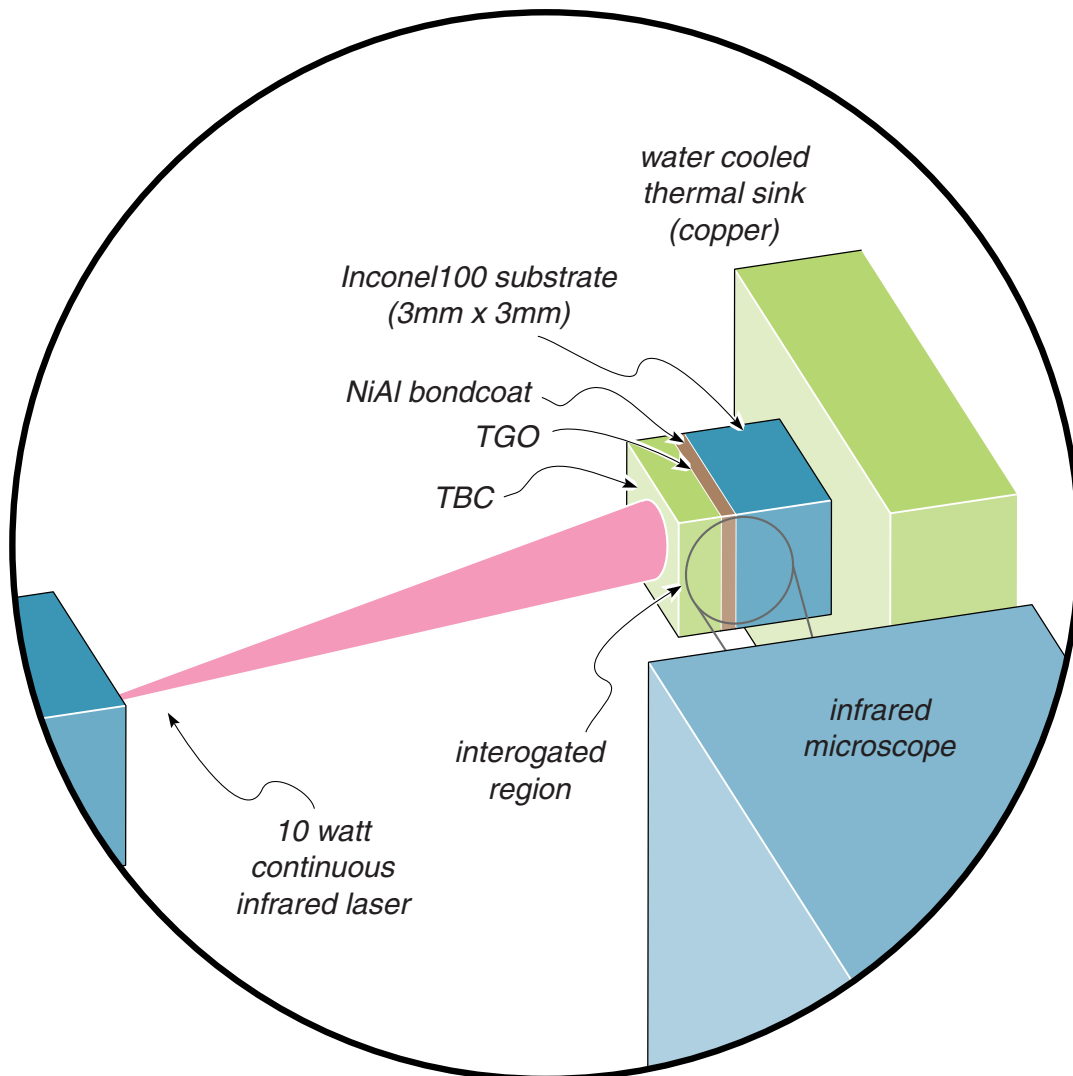


Figure 8

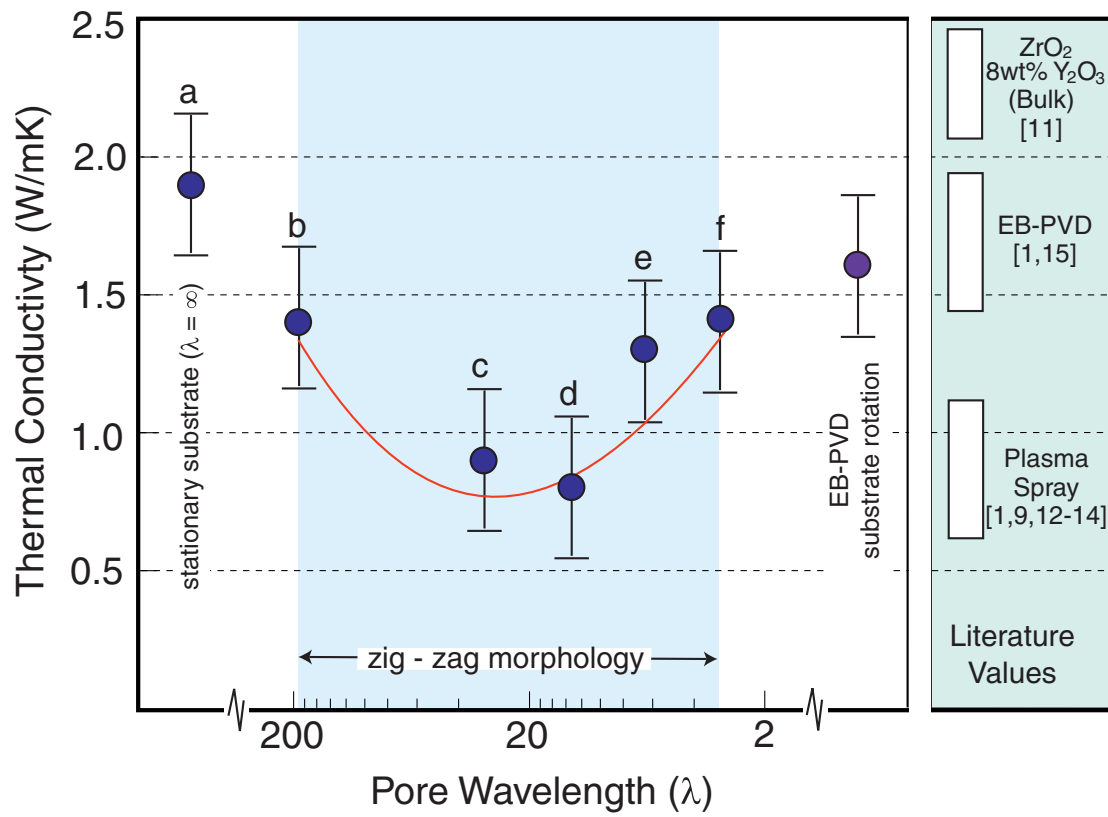


Fig. 9